10. D. W. Lea, G. T. Shen, E. A. Boyle, *Nature* **340**, 373 (1989).
11. A distribution coefficient is usually defined by an equation of the form: D_{Sr} = $(Sr/Ca)_{mineral}$/$(Sr/Ca)_{fluid}$, where $(Sr/Ca)_{mineral}$ and $(Sr/Ca)_{fluid}$ are the molar concentration ratios of these elements in the mineral and fluid, respectively.
12. W. L. McIntire, *Geochim. Cosmochim. Acta* **37**, 1209 (1973).
13. We calculated 2σ error estimates from the mean square of the residuals of a linear regression through the data presented in (*9*) for the coral genus *Porites*.
14. Sr and Ca concentrations were measured by isotope dilution on a Finnigan MAT 262 solid source mass spectrometer, using static Faraday collection. An exponential mass fractionation (*33*) correction for $^{84}Sr/^{86}Sr$ and $^{44}Ca/^{42}Ca$ was used, correcting to an assumed (*34*) natural $^{86}Sr/^{88}Sr$ = 0.1194 and an assumed (*33*) natural $^{42}Ca/^{44}Ca$ = 0.31221. Spike isotopic composition corrections were based on gravimetric determinations for Ca, and on non–fractionation-corrected TIMS determinations of the isotopic composition of the Sr spike. Results of 19 runs of Minnesota Isotope Laboratory standard ISC-1 Ca yielded an average $^{40}Ca/^{42}Ca$ = 151.030 ± 19 (2σ), whereas results of 10 runs of National Bureau of Standards (NBS) standard 987 Sr yielded an average $^{87}Sr/^{86}Sr$ = 0.710239 ± 10 (2σ).
15. Each Sr or Ca analysis constitutes between 50 and 100 individual mass spectrometric scans (isotopic ratios). A standard error (SE) of the mean is calculated for each analysis; these SEs are in turn propagated to determine the SE for the Sr/Ca ratio. "Average uncertainty" in the sense used here refers to the average (2σ) SE for all of the Sr/Ca analyses reported in this paper. "External reproducibility" as it is used here refers to two standard deviations of the population, where the population constitutes the mean values of several different determinations of the Sr/Ca ratio of a standard.
16. J. N. Weber and M. J. Woodhead, *J. Geophys. Res.* **77**, 463 (1972).
17. T. McConnaughey, *Geochim. Cosmochim. Acta* **53**, 151 (1989).
18. $\delta^{18}O$ is the normalized deviation, in parts per thousand, of the sample $^{18}O/^{16}O$ relative to standard mean ocean water (SMOW) (*35*).
19. We performed $\delta^{18}O$ analyses on a Finnigan MAT delta-E mass spectrometer. Average internal precision on the $\delta^{18}O$ analyses is reported at 0.07 per mil (2σ) on a typical 5-mg sample of coral. Five runs of standard NBS 18 yielded an average $\delta^{18}O$ (SMOW) = 7.18 ± 0.06 per mil (2σ), whereas results of nine runs of standard NBS 19 yielded somewhat poorer external reproducibility, with an average $\delta^{18}O$ (SMOW) = 28.75 ± 0.10 per mil (2σ).
20. The Sr/Ca temperature calibration made use of the $\delta^{18}O$ versus temperature calibration for the coral genus *Porites* generated by McConnaughey (*17*). This equation may be expressed as: $\delta^{18}O_c - \delta^{18}O_w = 0.594 - 0.209\,T$(°C), where $\delta^{18}O_c$ and $\delta^{18}O_w$ are the O isotopic compositions of the coral and seawater, respectively. The value of $\delta^{18}O_w$ for one seawater sample from the Amedee Lighthouse, Noumea, New Caledonia, calibration site was +0.52 ± 0.06 per mil (2σ). Average seawater $\delta^{18}O$ was assumed to be +0.6 per mil for this site based on published compilations.
21. W. S. Broecker and T. H. Peng, *Tracers in the Sea* (Lamont-Doherty Geological Observatory, Columbia University, New York, 1982).
22. D. J. Kinsman, *J. Sediment. Petrol.* **39**, 486 (1969).
23. G. W. Brass and K. K. Turekian, *Earth Planet. Sci. Lett.* **16**, 117 (1972).
24. ______, *ibid.* **23**, 141 (1974).
25. J. Murray and A. F. Renard, in *Challenger Reports* (Government Printer, London, 1891).
26. This coral sample (TX-6928) was radiocarbon dated at the Texas Radiocarbon Laboratory, University of Texas at Austin. The date is for a ^{14}C half-life of 5730 years. A stable isotope fractionation correction was not carried out and oceanic carbon reservoir corrections were not made. For the older value of the ^{14}C half-life of 5568 years, the age of this coral is 9870 ± 200 (2σ) radiocarbon years before present.
27. M. S. Halpert and C. F. Ropelewski, *Atlas of Tropical Sea Surface Temperatures and Surface Winds (National Oceanic and Atmospheric Administration Atlas #8*, U.S. Department of Commerce, Washington, DC, 1989).
28. F. Rougerie, B. Wauthy, J. Rancher, *C. R. Acad. Sci.*, in press.
29. D. Rind, D. Peteet, W. Broecker, A. McIntyre, W. Ruddiman, *Clim. Dyn.* **1**, 3 (1986).
30. R. L. Edwards, J. H. Chen, G. J. Wasserburg, *Earth Planet. Sci. Lett.* **81**, 175 (1987).
31. S. Epstein and T. Mayeda, *Geochim. Cosmochim. Acta* **4**, 213 (1953).
32. H. Craig and L. Gordon, in *Stable Isotopes in Oceanographic Studies and Paleotemperatures*, E. Tongiori, Ed. (Spoleto, Pisa, 1965), pp. 9–130.
33. W. A. Russell, D. A. Papanastassiou, T. A. Tombrello, *Geochim. Cosmochim. Acta* **42**, 1075 (1978).
34. A. O. Nier, *Phys. Rev.* **54**, 275 (1938).
35. H. Craig, *Science* **133**, 1833 (1961).
36. We are grateful to G. Shen for stimulating us to pursue improvements in the coral Sr/Ca ocean thermometer. We also thank T. Crowley, T. Quinn, C. Gallup, and R. Schultz for helpful comments. This work was made possible by the following National Science Foundation grants: EAR-8917103 (J.W.B. and W.E. Seyfried, Jr.), EAR-8904895 (R.L.E.), EAR-8904705 (R.L.E.), ATM-8921760 (R.L.E.), EAR-8904987 (F.W.T.), ATM-8904987 (F.W.T.), and EAR-9004762 (E.I.). Support for the TIMS analytical facility was made possible by NSF grant EAR-8817260 (R.L.E.), as well as funds from the University of Minnesota.

12 March 1992; accepted 20 May 1992

Maintenance of Strong Rotational Winds in Venus' Middle Atmosphere by Thermal Tides

Matthew Newman* and Conway Leovy

The cloud-level atmosphere of Venus takes little more than 4 days to complete one rotation, whereas the solid planet below has a 243-day period. Computer simulations of the circulation of the Venus middle atmosphere between 40 and 85 kilometers, as driven by solar radiation absorbed in the clouds, reproduce (i) the observed cloud-level rotation rate, (ii) strong vertical shears above and below the cloud tops, and (iii) midlatitude jets and strong poleward flow on the day side. Simulated circulations converge to yield nearly the same zonal winds when initialized with both stronger or weaker rotation rates. These results support the hypothesis that the observed cloud-top rotation rate is maintained by statistical balance between fluxes of momentum by thermal tides and momentum advection by mean meridional circulation.

Virtually the entire Venus atmosphere, from above the lowest scale height to well above the cloud tops (65 to 70 km), rotates much faster than the solid planet. Although the equatorial rotational speed of the solid surface is only 4 m s^{-1}, the atmospheric rotational speed reaches a maximum of approximately 100 m s^{-1} near the equatorial cloud-top level (65 to 70 km) (*1*). This phenomenon, known as superrotation, is the central dynamical problem of the Venus atmosphere. We report here the results of numerical simulations aimed at clarifying the mechanism for maintaining the equatorial cloud-top rotation.

Although the zonally symmetric Hadley circulation, which is thermally driven, can carry angular momentum upward, it transports this angular momentum to high latitudes and cannot maintain a maximum in equatorial angular momentum near cloud-top level. Waves are needed to counter this transport, as well as friction (*2*). Planetary waves arising from horizontal shear instability of the zonal flow (barotropic instability) could maintain the equatorial rotation by transporting angular momentum horizontally from midlatitudes toward the equator, but only if wave amplitudes are sufficiently large (*3*). Observational evidence for the required transport of eddy momentum by large amplitude planetary waves is lacking, however (*4*).

Alternatively, vertically propagating waves could provide the required momentum source. The relative motion between the rotating atmosphere and the pattern of solar heating, which has a maximum where solar radiation is absorbed in the cloud tops, drives diurnal and semidiurnal thermal tides that propagate vertically away from the cloud-top level. The effect of this wave propagation is to transport momentum vertically toward the cloud-top level at low latitudes and accelerate the mean zonal flow there. At higher altitudes, where much of the energy of the thermal tides is dissipated, these waves decelerate the mean zonal flow (*5–7*). We investigated the tidal mechanism using a numerical model that includes the zonally symmetric components of the flow and the two longest zonal waves. This model also allows us to address several outstanding problems posed by observations of Venus' middle atmosphere: (i) observed temperature distributions indicate that there are strong cyclostrophically bal-

Department of Atmospheric Sciences, University of Washington, Seattle, WA 98195.

*Present address: CIRES, University of Colorado, Boulder, CO 80309–0216.

anced midlatitude jets (7, 8), but winds inferred from cloud drifts indicate that jets are weak or absent (4); (ii) meridional winds derived from measurements of cloud drift are far stronger than those expected to result from thermal forcing of the Hadley circulation (4); (iii) dark bands in the cloud structure are frequently observed to spread poleward from the equator in the illuminated morning quadrant but not in the afternoon quadrant (9).

We used a semispectral primitive equation model with a zonal mean flow and zonal wavenumbers 1 and 2 (10). These waves correspond to the diurnal and semidiurnal tides, but they can also be excited by barotropic or baroclinic instability. Waves of higher wavenumbers and interactions between the waves are neglected; these terms may not be insignificant. Symmetry about the equator is assumed; therefore, the model applies to one hemisphere and covers altitudes from 30 to 110 km. At the lower boundary, the horizontal flow is fixed at a prescribed background rotation rate with no meridional velocity. Vertical wind can be nonzero there, but momentum transport from this boundary is negligible (10). Horizontal and vertical resolutions are 1.5° latitude and 1.5 km. Solar and thermal infrared heating, based on Venus observations and calculations, drive the model flow (11, 12). Dissipation is mainly by Rayleigh friction of the form $F_r = -K_r(\omega - \omega_0)$, where ω is the local angular velocity and ω_0 is the prescribed background angular velocity. The coefficient of Rayleigh friction is $K_r = k\{1 + \tanh[h^{-1}(z-z_0)]\}$, where z is altitude, and profile shape is specified through the constants $z_0 = 86.4$ km and $h = 10$ km (13). This form and the value $k = 0.579 \times 10^{-5}$ s^{-1} were chosen to produce strong dissipation above 85 km in order to absorb upward propagating waves and limit extreme flow velocities there, yet to give very weak Rayleigh friction below 70 km where $K_r < 0.04 \times 10^{-5}$ s^{-1}. We examine results only for the layer from 40 to 85 km. On the basis of short runs in which z_0 was raised, cloud-layer results do not appear to be sensitive to the Rayleigh friction. The model also has weak vertical diffusion, and very weak horizontal diffusion, which has a smoothing effect on the flow only at the two grid-points nearest the pole (14).

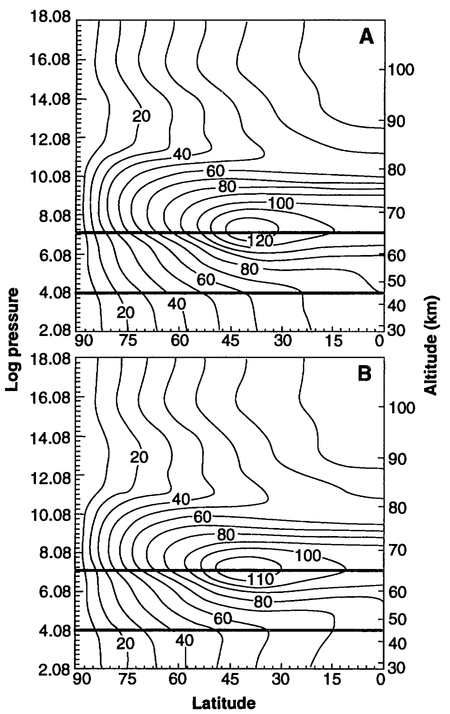

Fig. 1. Mean zonal winds from the simulation initiated with a uniform background rotation rate corresponding to 75 m s^{-1} on the equator (**A**), and for the same uniform background rotation initiated with an added shear component giving a maximum total rotational speed of 125 m s^{-1} (**B**). Both cases correspond to averages of the last 40 days of 300-day runs. The solid lines at 45 and 65 km represent the approximate vertical extent of the cloud layer; about half of the solar energy absorbed by the Venus atmosphere is deposited in this region. Height in atmosphere also shown as log of pressure (13).

We examine the importance of various mechanisms to the maintenance of the cloud-level superrotation, not the origin of the slower superrotation that occurs at lower levels, and report the results of two simulations carried out with uniform background angular velocity equivalent to an equatorial speed of 75 m s^{-1}. Flow with this angular velocity was the initial condition for one simulation. The initial condition for the other simulation was obtained by adding to this background rotation a horizontally uniform, cyclostrophically balanced component with zero additional zonal velocity at 30 and 110 km and a smooth increase to a maximum addition of 50 m s^{-1} at 65 km on the equator. This addition resulted in an initial flow with a maximum total speed of 125 m s^{-1}. Both cases were run for 300 simulated (Earth) days, by which time a statistically steady state was reached. The final state was not absolutely steady because of weak low-frequency oscillations of the waves and mean flow that had a dominant period of 40 days in each run. We present averages for the last 40 days of each run. Four other model runs, in which the background rotation or the vertical diffusion was decreased, or both, yielded qualitatively similar results.

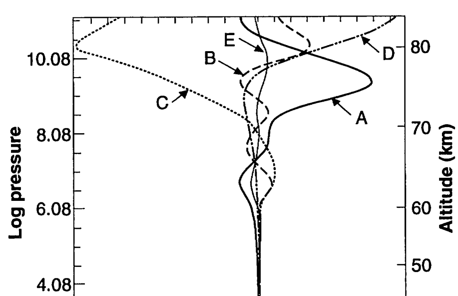

Fig. 2. Contributions to mean zonal flow acceleration on the equator from: (A) advection by zonal mean vertical velocity, (B) momentum flux convergence of the semidiurnal tide, (C) momentum flux convergence of the diurnal tide, (D) Rayleigh friction, (E) vertical diffusion. Averages are for the last 40 days of the 300-day simulation with initial sheared angular velocity.

In the resulting mean zonal flow for either initial state (Fig. 1) the equilibrated equatorial wind maximum was approximately 100 m s^{-1}, and a jet developed near 40° latitude. In general, both the cloud-level wind field and the vertical wind profile at low latitudes are broadly consistent with observations (1, 4, 8, 15). The equatorial wind maximum was maintained primarily by the convergence of vertical momentum transport by the semidiurnal tide, which caused an acceleration of approximately 0.6 m s^{-1} per day at the level of the jet on the equator (Fig. 2). Below the low-latitude zonal wind maximum, the vertical wind profile was maintained by approximate balance between the momentum flux of the two tides and vertical advection by the vertical velocity of the weak Hadley circulation. Above 70 km, the semidiurnal tide strongly decelerated the flow until the resulting shear was maintained by the balance between wave deceleration and vertical advection due to the Hadley cell updraft.

The diurnal tide contributed to the acceleration of the mean zonal flow below the wind maximum, primarily by transporting angular momentum horizontally from the region of the midlatitude jet toward lower latitudes. This transport, which resulted in large part from the interaction between radiatively damped vertically propagating and vertically trapped components of the tide (5), smooths the zonal wind profile between the midlatitude jets and the equator and provides a consistent explanation for the remarkable uniformity of the observed zonal winds at latitudes below 40° (4). We verified this profile-smoothing role of the tides by running the model with the sheared angular velocity profile added to the background angular velocity in the zonally symmetric mode (no waves). In this run, the model did not reach a statistically steady state because of the absence of tidal momentum fluxes, but the equatorial wind speed decreased to near the background rotation rate as a midlatitude jet developed that was stronger and higher in latitude throughout the run than in runs with tides. This result is consistent with theoretical

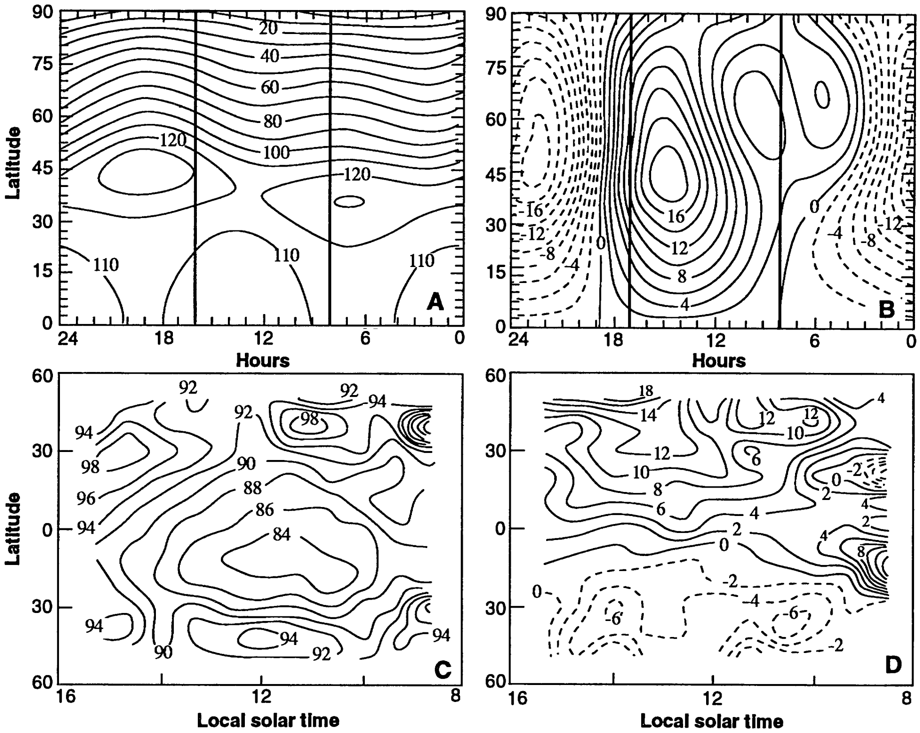

Fig. 3. Comparison of model distributions of cloud-top zonal and meridional winds with local time (**A** and **B**) and with distributions derived from cloud-drift measurements (**C** and **D**). Model results are averages from the last 40 days of the 300-day simulation with initial sheared angular velocity. All zonal winds are retrograde (in the sense of the planetary rotation), and positive meridional winds are northward (upward in the figure). The model distributions cover all local times but only the northern hemisphere, whereas the cloud-drift measurements cover both hemispheres but only local times of 0800 to 1600. Both model and observations show zonal wind minima near local noon and maximum poleward meridional flow in the afternoon.

predictions of the latitude and strength of the jet (*16*). This zonally symmetric jet was strongly barotropically unstable; however, momentum transport of the diurnal tide weakened the instability so that jet instability did not generate significant planetary-scale waves.

Tides can also act to modify the Hadley circulation through divergences of their meridional and upward heat fluxes. At the equator, the vertical convergence of the upward heat flux in our model compensated part of the zonally averaged solar heating in the cloud-top region. This effect, which had been previously estimated to be small (*6*) and has been neglected in some models (*17*), was significant and reduced the mean equatorial cloud-level updraft by half, as compared to the zonally symmetric run. Thus, the tides acted to maintain the mean zonal flow at cloud-top level in two ways: directly, through tidal fluxes of angular momentum, and indirectly, by reducing the thermal forcing of the Hadley cell.

The temperature pattern of the semidiurnal tide is broadly consistent with Pioneer Venus temperatures and with linear tidal theory between the cloud-top level and 80 km (*18, 19*). The vertical wavelength of the semidiurnal tide was about 20 km, and the temperature amplitude was largest at low latitudes, but significant amplitude extended to the latitude of the jet. The relatively large midlatitude tidal amplitude in both the observations and the model can be attributed to the effect of the jet on the tidal modes (*19*). Both observed and modeled diurnal tides have largest amplitude near the jet latitude; this result appears to be caused by the large vertically trapped component of the diurnal tide.

At cloud-top level, the model zonal wind has a distinct minimum during daytime such that the midlatitude jet is substantially diminished from the zonal mean value. The daytime meridional wind, on the other hand, is strongly poleward and is a maximum in early afternoon (Fig. 3). This is a robust result that is consistent with both the near absence of midlatitude jets and the strong meridional winds deduced from cloud drifts. Cloud drifts can be measured only during the period from about 0800 to about 1600 hours local time, but they have been used to infer the strength of zonally averaged zonal and meridional winds (*4*). As shown by these results, this method can lead to spurious estimates. The magnitude and phase of the diurnally varying meridional winds are consistent with small-probe measurements from Pioneer Venus (*15*) and can account for the poleward spreading of the dark horizontal band in the cloud-top dark markings consistently observed during the morning.

Spectral analyses of model results also show nontidal wave components: a strong wavenumber 2 component with a period of 2.6 days, and a weak wavenumber 1 component with the same angular phase speed and period of 5.2 days. These are confined mainly to the midlatitude region below the cloud-top level. They arise from baroclinic and barotropic instabilities of the zonal mean flow in this part of the atmosphere. These features may be related to a 5.2-day spectral feature of wavenumber 1 that has been detected in cloud-level temperature data, cloud-top ultraviolet brightness variations, and cloud-drift winds (*20*). The model dominance of a wavenumber 2 feature with a 2.6-day period instead of the 5.2-day wave 1 may be a consequence of the omission of wave-wave interactions or the model structure of the background atmosphere. To check the latter possibility, we repeated the simulations described above but with background angular velocity corresponding to an equatorial speed of 60 m s^{-1} and obtained similar but somewhat weaker cloud-top rotational winds and a somewhat stronger 5.2-day wave. These waves do not contribute to maintenance of the zonal mean flow near the equator, but in mid- to high latitudes the 2.6-day wave does act to transport momentum from the middle to lower cloud region, thereby influencing high-latitude zonal mean temperature and wind.

Our model converges from different initial conditions to a middle atmosphere zonal wind structure resembling that observed, and the results provide consistent explanations for other puzzles posed by the observations. Thus, the results seem to capture the essential role of thermal tides in maintaining the rotational wind structure in the region from 40 to 80 km. Several other observed features of the Venus atmosphere circulation remain unexplained. These include the wave structure, the relatively high temperature of the polar cloud-top region, and the critically important background rotation. Plausible mechanisms for maintaining a background rotation rate in the lower atmosphere include momentum flux due to convectively generated internal gravity waves or to the "moving flame" mechanism involving viscous wave propagation (*21*), but neither of these has been demonstrated quantitatively.

REFERENCES AND NOTES

1. G. Schubert, in *Venus*, D. M. Hunten *et al.*, Eds. (Univ. of Arizona Press, Tucson, AZ, 1983), chap. 21; V. V. Kerzhanovich and M. Ya. Marov, *ibid.*,

chap. 22; M. Newman *et al.*, *J. Atmos. Sci.* **41**, 1901 (1984).
2. V. P. Starr, *The Physics of Negative Viscosity Phenomena* (McGraw-Hill, New York, 1968); R. Hide, *J. Atmos. Sci.* **26**, 841 (1969).
3. P. J. Gierasch, *J. Atmos. Sci.* **32**, 1038 (1975); W. B. Rossow and G. P. Williams, *ibid.* **36**, 377 (1979).
4. S. S. Limaye, C. Grassotti, M. J. Kuetermeyer, *Icarus* **73**, 193 (1988); W. B. Rossow, A. D. Del Genio, T. P. Eicheler, *J. Atmos. Sci.* **47**, 2053 (1990).
5. S. B. Fels and R. S. Lindzen, *Geophys. Astrophy. Fluid Dyn.* **6**, 149 (1974); V. Ramanathan and R. D. Cess, *Icarus* **25**, 89 (1975).
6. C. B. Leovy, *Icarus* **69**, 193 (1987).
7. R. L. Walterscheid *et al.*, *J. Atmos. Sci.* **42**, 1982 (1985).
8. C. B. Leovy, *ibid.* **30**, 1218 (1973); P. J. Valdes, thesis, Oxford University (1985). Cyclostrophically balanced zonal winds correspond to a balance between the equatorward component of the centrifugal acceleration of the winds and the poleward component of the pressure gradient force per unit mass.
9. L. D. Travis *et al.*, *Science* **203**, 781 (1979).
10. J. R. Holton and W. Wehrbein, *Pure Appl. Geophys.* **118**, 284 (1980).
11. M. Tomasko, in *Venus*, D. M. Hunten *et al.*, Eds. (Univ. of Arizona Press, Tucson, AZ, 1983); D. Crisp, thesis, Princeton University, Princeton, NJ (1983).
12. N. L. Baker and C. B. Leovy, *Icarus* **69**, 202. We adapted the heating formulation of Baker and Leovy but modified it to prevent forcing of static instabilities.
13. Height values given here are the approximate equivalent to geometric height given as the negative of the log of the atmospheric pressure divided by the surface pressure.
14. M. Newman, thesis, University of Washington, Seattle, WA (1991). The model follows that of Baker and Leovy (*12*), with the exception of the features described above and: (i) the basic-state vertical profiles of temperature, specific heat, and the standard static stability, which were not mutually consistent in the Baker-Leovy model, have been corrected; (ii) the boundary condition at the pole was changed to allow nonzero values of angular velocity there.
15. C. C. Counselman *et al.*, *J. Geophys. Res.* **85**, 8026 (1980).
16. I. M. Held and A. Y. Hou, *J. Atmos. Sci.* **32**, 1038 (1980); A. Y. Hou, *ibid.* **41**, 3437 (1984).
17. A. Y. Hou *et al.*, *J. Atmos. Sci.* **47**, 1894 (1990).
18. J. T. Schofield and F. W. Taylor, *Q. J. R. Meteorol. Soc.* **109**, 57 (1983); J. B. Pechman and A. P. Ingersoll, *J. Atmos. Sci.* **41**, 3290 (1984); L. S. Elson, *ibid.* **40**, 1535 (1983).
19. S. B. Fels, *J. Atmos. Sci.* **43**, 2757 (1986).
20. A. D. Del Genio and W. B. Rossow, *ibid.* **47**, 293 (1990).
21. A. Hou and B. Farrell, *ibid.* **44**, 1049 (1987); G. Schubert and J. A. Whitehead, *Science* **163**, 71 (1969); C. Covey, R. L. Walterscheid, G. Schubert, *J. Atmos. Sci.* **43**, 3273 (1986).
22. This research was supported by the Planetary Atmospheres Program of the Solar System Exploration Division of the National Aeronautics and Space Administration. Simulations were carried out on the Cray Y-MP computer at the San Diego Supercomputer Facility of the National Science Foundation, whose provision of computer time is gratefully acknowledged.

3 March 1992; accepted 16 June 1992

Elasticity of α-Cristobalite: A Silicon Dioxide with a Negative Poisson's Ratio

Amir Yeganeh-Haeri, Donald J. Weidner, John B. Parise

Laser Brillouin spectroscopy was used to determine the adiabatic single-crystal elastic stiffness coefficients of silicon dioxide (SiO_2) in the α-cristobalite structure. This SiO_2 polymorph, unlike other silicas and silicates, exhibits a negative Poisson's ratio; α-cristobalite contracts laterally when compressed and expands laterally when stretched. Tensorial analysis of the elastic coefficients shows that Poisson's ratio reaches a maximum value of −0.5 in some directions, whereas averaged values for the single-phased aggregate yield a Poisson's ratio of −0.16.

The three distinct crystalline forms of SiO_2—quartz, tridymite, and cristobalite—occur widely in nature. Because of the broad technological applications and sheer abundance of quartz, its physical properties have been extensively studied; yet comparatively, there is little information available on the physical properties of cristobalite and tridymite. All three polymorphs of SiO_2 form complex three-dimensional, corner-linked networks of rigid SiO_4 tetrahedra. Furthermore, each of these crystalline forms has a high-temperature (β) and a low-temperature (α) modification (*1, 2*).

We measured the single-crystal elastic properties of SiO_2 in the α-cristobalite structure under ambient conditions (*3*). We find that α-cristobalite exhibits a negative Poisson's ratio, contracting laterally when compressed and expanding laterally when stretched. Foams and two-dimensional honeycomb structures, that is, amorphous materials, and some elements such as As and Sb, also have negative Poisson's ratios (*4, 5*), but other minerals apparently do not.

Center for High Pressure Research and Department of Earth and Space Sciences, State University of New York at Stony Brook, Stony Brook, NY 11794.

In an isotropic medium, Poisson's ratio (ν) is defined as the quotient of lateral contraction divided by longitudinal extension. Solids usually contract laterally when stretched and expand laterally when compressed, resulting in a positive Poisson's ratio. Poisson's ratio falls between 0.20 and 0.27 for most crystalline compounds and hard metals, has values between 0.30 and 0.40 for most soft metals, and is exactly 0.5 for liquids. Albeit it is counterintuitive that a solid should have a negative Poisson's ratio, according to the theory of elasticity the allowable range for Poisson's ratio in an isotropic medium is between +0.5 and −1.0 (*6, 7*). These limits can be understood in terms of the relation between the bulk modulus (K) and the shear modulus (μ) of a solid, expressed as

$$\nu = (3K - 2\mu)/(6K + 2\mu) \qquad (1)$$

If the solid is incompressible, that is, as K approaches infinity, it can be seen from Eq. 1 that ν approaches the upper limit of 0.5. In this type of solid, the bulk modulus is substantially larger than the shear modulus. For example, in liquids the shear modulus is zero; hence Poisson's ratio is exactly 0.5. Conversely, as K approaches zero, in the case of an infinitely compressible solid, ν tends toward −1.0. In this type of solid, the shear modulus far exceeds the bulk modulus. Other extraordinary behavior is also predicted to occur in compounds with a negative Poisson's ratio. For instance, as the Poisson's ratio approaches the lower limit of −1.0, the material's fracture toughness and its resistance to indentation are greatly enhanced. In other words, despite being pliant, the material can become tough (*4, 5*, and references therein). Materials exhibiting a negative Poisson's ratio also have a large potential for applications as shock absorbers and fasteners.

We determined the single-crystal elastic properties of α-cristobalite using Brillouin spectroscopy (*8*). The experiments were carried out on a natural single crystal from the Ellora Caves of Hyderabad, India. The specimen was 200 μm in maximum dimension, colorless, and transparent, and its shape was a perfect octahedron. A total of 58 compressional and shear acoustic velocities in 27 distinct crystallographic directions were used to constrain the velocity surface (Fig. 1). The velocity surface of α-cristobalite is such that one of the shear (S) modes travels at a faster velocity than the corresponding compressional (P) wave (*9*). This velocity surface was inverted to determine the six independent elastic stiffness coefficients that characterize tetragonal α-cristobalite, space group $P4_12_12$ (Table 1) (*10*).

The large magnitude of the six elastic compliance coefficients (*11*) strongly reflects the pliant nature of the α-cristobalite framework (Table 1; Fig. 2A). This framework is highly anisotropic. The c axis, with a linear compressibility of β_c = 2.73 MPa^{-1}, is much more compressible than the a axis for which β_a = 1.77 MPa^{-1}. The α-cristobalite structure is also more rigid than it is incompressible; the shear modulus is approximately 2.4 times the bulk modulus (Table 1). Because the Si–O forces are